An Analog VLSI Model of Muscular Contraction

Tina A. Hudson, *Member, IEEE*, Julian A. Bragg, *Member, IEEE*, Paul Hasler, and Stephen P. DeWeerth, *Member, IEEE*

***Abstract*—We have developed analog VLSI circuits to model the behavior demonstrated by biological sarcomeres, the force generating components of muscle tissue. The circuits are based upon the mathematical description of crossbridge populations developed by A. F. Huxley. We have implemented the sarcomere circuit using a standard 1.2-μm process, and have demonstrated the nonlinear transient behaviors exhibited by biological muscle.**

***Index Terms*—Sarcomere model, Huxley's crossbridge model, analog VLSI, neuromorphic engineering.**

I. Introduction

NATURE has developed a unique set of solutions for controlling movement in a wide variety of situations. Skeletal muscle, the actuator used in voluntary movements, is capable of performing both fine motion control, such as that required in writing and speech, and large, powerful movements, such as that associated with running and jumping. This actuator is based upon a modular architecture that uses different combinations of a small set of building blocks with different properties to create a large variety of muscle types, facilitating the amazing versatility found in biological systems [1]. In addition to this versatility, by using arrays of these building blocks, muscle achieves efficient actuation with an excellent power-to-weight ratio [2]. By exploiting the underlying architecture of muscle, it is possible to improve the versatility and efficiency of engineered motion-control systems.

Exploitation of the biological organizational principles provides a foundation for developing a *biomorphic actuator* (an actuator whose structure and function closely resembles its biological counterpart) and associated control circuitry. Such an actuator would have the potential to be used in multiple engineering applications. An actuator that had the same input-output characteristics as biological muscle could be used to produce a limb prosthesis that mimicked biological movements in a more natural manner. A biomorphic actuator could also be used in conjunction with functional electrical stimulation systems (systems used to artificially stimulate muscle tissue) to investigate their effectiveness at controlling muscle tissue in a biological fashion. We could also use such actuators in autonomous robots, which require efficient, lightweight actuators that can perform a diverse set of complex tasks.

The first step to producing a biomorphic actuator is to produce a *biomorphic model* of muscle actuation that will ultimately be used to control a standard linear actuator or an array of linear actuators. By basing our implementation on a model that is founded upon the underlying biological processes, the biomorphic model is capable of producing some of the more subtle nonlinear properties of muscle such as history dependence and the complex interaction between force, length, and velocity. Additionally, the biomorphic model may be more likely to produce appropriate behaviors when the model is simulated in a new regime of operation that biological experimentation has not identified.

We have developed a biomorphic model using nonlinear, low-power circuitry that demonstrates many of the characteristics of biological actuation. Muscle demonstrates nonlinear relationships between force, neural stimulation, length, and velocity. In order to implement these features in the most efficient manner, we employ nonlinear, analog circuitry. Prosthetic and autonomous robotics applications require low-power systems which are portable, demanding low-power circuitry for the biomorphic model. Therefore, we have exploited a tool that has been proven to be useful for modeling low-power neural systems. Neuromorphic, analog very large-scale integrated (VLSI) circuit technology [3] utilizes large arrays of analog transistors operating in their subthreshold regime. This type of circuitry has many advantages including: 1) the ability to obtain nonlinear behaviors demonstrated by biology using a small number of transistors; 2) low currents, associated with subthreshold operation, which produce low-power implementations; and 3) the ability to be used to implement many components operating in parallel, mimicking the architecture governing neural systems. The parallel nature of the VLSI circuits allows our biomorphic model to operate in real-time, which is essential to interact with the real world.

In this paper, we will present the nonlinear characteristics associated with biological actuation and describe a circuit implementation of these characteristics. This circuit has been fabricated and tested, and experimental results are presented.

II. Description of Biological Actuation

Mammalian skeletal muscle has a hierarchical structure, as shown in Fig. 1 [1]. Whole muscles are comprised of a parallel array of muscle fibers, which contain a parallel array of myofibrils. The myofibrils contain sarcomeres (the force generating components of muscle) organized both in series and in

Manuscript received August 14, 2001; revised December 26, 2002. This work was supported by the National Science Foundation under Grant 9872759 and by a Biomedical Engineering Research Grant from the Whitaker Foundation. This paper was recommended by Associate Editor A. Rodriguez-Vazquez.

T. A. Hudson is with the School of Electrical and Computer Engineering, Laboratory for Neuroengineering, Georgia Institute of Technology, Atlanta, GA 30332 USA, and also with the Deptartment of Electrical and Computer Engineering, Rose-Hulman Institute of Technology, Terre Haute, IN 47803 USA (e-mail: tina.hudson@rose-hulman.edu).

J. A. Bragg is with the School of Electrical and Computer Engineering, Laboratory for Neuroengineering, Georgia Institute of Technology, Atlanta, GA 30332 USA, and also with the Department of Physiology, Emory University, Atlanta, GA 30303 USA.

P. Hasler, and S. P. DeWeerth are with the School of Electrical and Computer Engineering, Laboratory for Neuroengineering, Georgia Institute of Technology, Atlanta, GA 30332 USA.

Digital Object Identifier 10.1109/TCSII.2003.813593

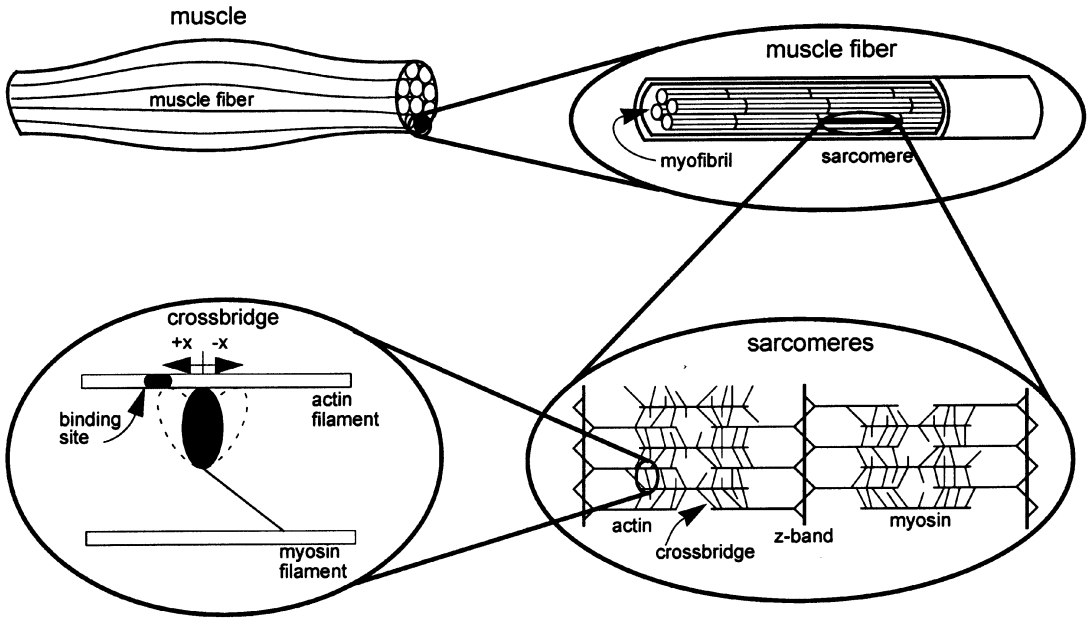

Fig. 1. The component parts of mammalian skeletal muscle: muscles are made up of parallel fibers, each of which consists of many myofibrils in parallel. The myofibrils consist of sarcomeres in series and parallel. Sarcomeres, the subunit being modeled in this work, are the fundamental force-generating elements. They are made up of parallel actin and myosin filaments, with myosin crossbridges stretching between them.

parallel. Within each sarcomere are actin and myosin filaments, which provide much of the structure of the muscle, and crossbridges (the heads of the myosin filament) that stretch between the actin and myosin [4]. The crossbridges rotate through positions of lower potential energy causing the actin and myosin filaments to slide relative to one another, resulting in muscle contraction.

All force is produced by the spring-like characteristics of crossbridges [4]. Similar to a spring's natural length, where its force is equal to zero, a crossbridge has an equilibrium position where it cannot produce force (see Fig. 1). A detached crossbridge will attach to the actin filament some distance away from it's equilibrium position. As a consequence of being a part of a distributed system, the attached crossbridge can be moved to positions positive or negative to the equilibrium position by the sliding of the filaments. Like a spring, each attached crossbridge contributes a force that is proportional to the distance it is stretched from its equilibrium position. The total force of the muscle is the sum of all the individual crossbridge forces.

The unique force characteristics demonstrated by muscle are mediated by the attachment, detachment, and movement of the crossbridges. Muscle force has a nonlinear relationship with the muscle length and the velocity of stretch or contraction [5] (shown in Fig. 2), which enhances both stability and performance [6]. As the muscle actively shortens [see Fig. 2(a)], force falls exponentially, saturating at a lower steady-state level. Faster contraction velocities result in lower steady-state force levels (dashed line). This characteristic occurs because the contraction pulls many crossbridges to positions negative to their equilibrium position, where they resist contraction, producing a negative force contribution. However, these crossbridges soon detach, preventing the whole sarcomere from producing a negative net total force. As the muscle lengthens

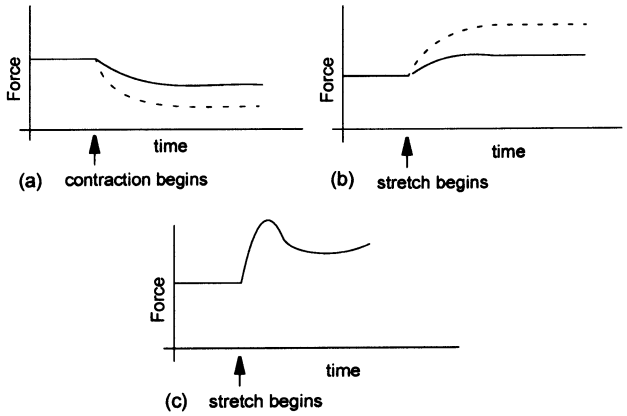

Fig. 2. The nonlinear dependency of biological muscle force on muscle velocity during (a) a constant velocity contraction and (b) a constant velocity stretch. In both cases, the dashed lines indicate higher velocities. (c) The force output of biological muscle during an extremely high velocity stretch, demonstrating the nonlinear property of yielding, which is critical in determining a muscle's initial response to an applied length perturbation.

due to an externally applied force greater than the muscle force [see Fig. 2(b)], the muscle force increases and saturates at a higher steady-state level because crossbridges are being pulled to positions positive to their equilibrium position, increasing the force contribution of these crossbridges. Faster lengthening velocities result in higher steady-state muscle force levels (dashed line).

The transient response to high velocity stretches is highly nonlinear [5]. The force rapidly increases to a much higher value and then falls to a new steady-state value [see Fig. 2(c)]. This response is due to crossbridge detachment at positions far from the equilibrium position. The initial linear response of the muscle is known as the short range stiffness (for short operating ranges,

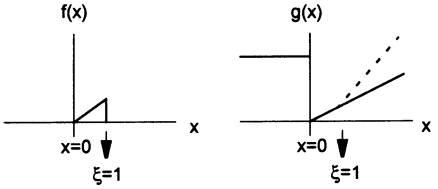

Fig. 3. Crossbridge attachment ($f(x)$) and detachment ($g(x)$) rates as a function of x, with the solid lines indicating the curves used by Huxley [4], and the dashed line indicating the modification made by Zahalak [8]. $x = 0$ denotes the equilibrium position, and $\zeta = 1$ denotes the maximum length at which an unattached crossbridge can attach. We will refer to the region between these two points as the first bond length.

the stiffness is very high) and the decline in force is known as yielding. Many neuroscientists assume that the role of short range stiffness is to stabilize the limb posture in response to unexpected perturbations [7], [5]. Because this response occurs before the neural feedback mechanisms can begin to operate, it is considered an important nonlinear response for muscle tissue.

The length of the sarcomere also plays a major role in determining its total force production by changing the total number of crossbridges available for attachment [1]. When the sarcomere is at longer and shorter lengths, fewer crossbridges are available for binding, which diminishes the maximum force production. The resulting force–length relationship has an optimal region for producing the maximum force that linearly declines for longer and shorter lengths.

III. Huxley's Mathematical Model

The nonlinear properties of muscular contraction were captured by a mathematical model developed by Huxley [4]. Each sarcomere has thousands of crossbridges, facilitating the study of sarcomere mechanics using a statistical population of crossbridges. If $z(x,t)$ is the percentage of crossbridges that are at a distance x from their binding site at a given time t, then $n(x,t)$ represents the percentage of $z(x,t)$ that are attached. This formula incorporates important mechanical and chemical elements involved in sarcomere actuation, such as the velocity at which the actin and myosin filaments slide relative to one another and the crossbridge binding rates for attachment and detachment.

The equation describing $n(x,t)$ is

$$\frac{\partial}{\partial t}n(x,t) = f(x)(1 - n(x,t)) - g(x)n(x,t) + v(t)\frac{\partial}{\partial x}n(x,t) \tag{1}$$

where $f(x)$ and $g(x)$ are the binding and unbinding rates of the crossbridges and $v(t)$ is the contraction velocity. The $f(x)(1 - n(x,t))$ term represents the rate at which unattached crossbridges will attach. The $g(x)n(x,t)$ term denotes the rate at which attached crossbridges will detach. As the sarcomere is stretched or shortened, the actin and myosin filaments slide with respect to one another, causing attached crossbridges to move to different position. The term $v(t)(\partial/\partial x)n(x,t)$ calculates this movement of crossbridges as a function of the velocity of stretch or shortening.

Huxley hypothesized that the attachment and detachment rates ($f(x)$ and $g(x)$) vary with x due to the molecular orientations of the actin and myosin filaments [4]. These variations are depicted in Fig. 3. A crossbridge can only attach over a finite distance, h, called a single bond length. The parameter x is often normalized by the bond length as follows, $\zeta = x/h$, which relates x to a known distance in the sarcomere. Once the crossbridge is attached, movements in the sarcomere can stretch the crossbridge to positions where $\zeta > 1$ or $\zeta < 0$. However, this movement increases the energy in the state of the crossbridges, causing an increase in the detachment rate. The original Huxley model overestimated the forces during stretches and did not exhibit yielding at high velocities. Zahalak corrected this problem by modifying the detachment rate (shown by the dashed line in Fig. 3). The spatial dependence of the rate constants has not been experimentally measured; however, the form developed by Zahalak produces simulation data that match well to the biological data [8].

Assuming the crossbridge is linearly elastic, its force contribution can be calculated as the stiffness of the crossbridge multiplied by its distance away from the equilibrium position. The total force production for the entire sarcomere is the sum of the force contributions of each attached crossbridge, which is mediated by the following equation:

$$F(t) = K\int_{-\infty}^{\infty}(n(x,t)\cdot x)dx \tag{2}$$

where K is a scaling factor that represents the stiffness of the crossbridges.

The first order partial differential equation, (1), is difficult to implement in circuits because of the continuous nature of the spatial variable x. The method of lines is a numerical procedure that converts a partial differential equation into a set of ordinary differential equations by discretizing one of the independent variables using a finite difference equation [9]. We have applied this method to the spatial variable to simplify the circuit implementation. We augmented (1) by dividing x into k spatial bins, where each bin represents some range of x values. The resulting equation for a single bin is

$$\frac{d}{dt}n_i(t) = f_i(1 - n_i(t)) - g_i n_i(t) + v(t)\left(\frac{n_{i+1}(t) - n_i(t)}{x_{i+1} - x_i}\right) \tag{3}$$

where i is the bin number in the range 0 to $k-1$, and the partial derivative of n with respect to x is replaced by the the *right difference* equation of attached crossbridges in neighboring bins. In each of the difference equations, n_i represents the number of attached crossbridges in the ith bin and x_i represents the x value corresponding to the center of the bin. The constants f_i and g_i correspond to the value of $f(x)$ and $g(x)$ evaluated at x_i.

The force is calculated by a discretized version of (2)

$$F(t) = \sum_{i=0}^{k-1} n_i(t)\cdot x_i \cdot \left(\frac{x_{i+1} - x_{i-1}}{2}\right) = \sum_{i=0}^{k-1} n_i(t)\cdot w_i \tag{4}$$

where, for the ith bin, n_i represents the number of attached crossbridges in that bin, x_i represents the x value at the center of the bin, and $(x_{i+1} - x_{i-1})/2$ represents the bin width. Because $n_i = 0$ at $i = -1$ and $i = k$, the force contribution at these

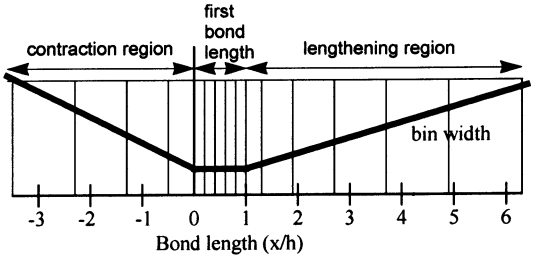

Fig. 4. Nonuniform bin distribution scheme, which retains a force–velocity curve matching that seen in biological muscle while reducing the number of bins required to implement the model. Bin density is highest in the first bond length, and reduces as bond length increases in the positive and negative directions.

bin positions is equal to zero. The force can be rewritten as a weighted sum of the distribution of attached crossbridges, where the weight of each bin is given by $w_i = x_i \cdot ((x_{i+1} - x_{i-1})/(2))$.

A major concern in developing the implementation of the sarcomere model is the trade-off between circuit size and biological accuracy. Although discretizing the spatial portion of the partial differential equation makes the circuit tractable, the implementation now requires a subcircuit for every spatial bin. Therefore, it is necessary to optimize the biological accuracy against the number and distribution of spatial bins. Prompted by the manner in which Huxley's model calculates crossbridge movement, we found that a nonlinear distribution of bins, shown in Fig. 4, with more bins of a smaller width in and near the first bond length $(0 > \zeta > 1)$, produced a force–velocity relationship that closely resembled the continuous solution [10], [11]. We performed mathematical simulations of the force–velocity relationship using a discrete representation of the continuous solution to Huxley's model. Using sixteen bins, these simulations demonstrated a two percent variation from the continuous solution over twenty percent of the input range. The highest observed variation was four percent for large velocity inputs. This nonlinear grid has been discussed in more detail in [10] and [11].

IV. Model Sarcomere Circuit Description

We implemented the Huxley model of sarcomere actuation using sixteen bins coupled together by circuits implementing the velocity term. By carefully setting the parameters among the bins, we created a nonlinear distribution of bin widths. This section will detail the circuit implementation of a single bin, the parameter distribution among the array of bins, and the circuits calculating the velocity from a differential length input and the force–length relationship.

A. Single Bin Implementation

The bold circuit elements in Fig. 5 comprise the circuit schematic for a single bin. Each of the bin circuits are operated in the subthreshold regime in order to 1) maximize power efficiency; 2) enable low frequency operation to mimic muscular time constants without requiring large, off-chip capacitors; and 3) utilize the exponential transconductance in this regime to simplify the parameter distribution. The capacitor voltage, V_{n_i} encodes the value of $n_i(t)$. This value is computed via the integration of a set of currents representing the individual terms on the right side of (3). Two transconductance amplifiers (TA_1 and TA_2) are used to generate currents I_{f_i} and I_{g_i}, which encode the attachment and detachment terms, $f_i(1 - n_i(t))$ and $g_i n_i(t)$, respectively. The voltages $f_{\mathrm{bias}\,i}$ and $g_{\mathrm{bias}\,i}$ encode the attachment rate constant and the detachment rate constant, respectively. Both of these values are set for each bin as a function of the crossbridge position, x_i. They set the transconductance of the TAs, and are programmed to values that ensure the TAs operate in the subthreshold regime. The relationship between the differential input voltage and output current of an TA operating in the subthreshold regime is of the form

$$I_{\mathrm{out}} = I_b \tanh\left(\frac{\kappa(V_+ - V_-)}{2U_t}\right) \tag{5}$$

where I_b is the bias current of the TA, U_t is the thermal voltage equal to $(kT)/q$, and κ is the gate efficiency constant [3]. If $(V_+ - V_-) < 200$ mV, (5) can be approximated as a linear relationship between $(V_+ - V_-)$ and I_{out}, shown below.

$$I_{\mathrm{out}} = I_b\left(\frac{\kappa(V_+ - V_-)}{2U_t}\right). \tag{6}$$

If $I_{f\,\mathrm{bias}_i}$ is defined as the bias current that results from the voltage f_{bias_i} and $I_{g\,\mathrm{bias}_i}$ is defined as the current that results from the voltage g_{bias_i}, then I_{f_i} and I_{g_i} can be written as follows.

$$I_{f_i} = \frac{I_{f\,\mathrm{bias}_i}\kappa}{2U_t}(V_\alpha - V_{n_i}) \tag{7}$$

$$I_{g_i} = \frac{I_{g\,\mathrm{bias}_i}\kappa}{2U_t}(V_{\mathrm{ref}} - V_{n_i}) \tag{8}$$

where V_α and V_{ref} represent the maximal and minimal fraction of crossbridges (1 and 0 respectively) that can be attached in a given bin. If $I_{f\,\mathrm{bias}_i}$ and $I_{g\,\mathrm{bias}_i}$ are equal to f_i and g_i in (3), then (7) and (8) correspond to the attachment rate $(f_i(1-n_i(t)))$ and detachment rate $(g_i n_i(t))$ terms.

To ensure that $(V_+ - V_-)$ is less than 200 mV for each TA, $V_\alpha - V_{\mathrm{ref}} \leq 200$ mV. If $V_\alpha > V_{\mathrm{ref}}$ (indicating activation of the sarcomere) and $f_{\mathrm{bias}_i} > g_{\mathrm{bias}_i}$, the node voltage, V_{n_i}, will increase until it reaches V_α. If $f_{\mathrm{bias}\,i} < g_{\mathrm{bias}\,i}$, V_{n_i} will remain at V_{ref}. When the sarcomere is not activated $(V_\alpha = V_{\mathrm{ref}})$, all node voltages remain at V_{ref}.

The velocity-dependent term in (3) is implemented using a complementary pair of unidirectional delay lines. One delay line calculates crossbridge movement from bins on the right to bins on the left, which occurs during contraction. The other delay line calculates crossbridge movement in the opposite direction, which occurs during lengthening. To appropriately control each of the delay lines, we transformed the velocity input by multiplying it by two unit step functions, $u(t)$ and $u(-t)$ for the contraction and lengthening components respectively. In the original Huxley equation, positive velocities represent contraction and negative velocities represent lengthening [4]. To eliminate the need for negative input voltages, we use these half-wave rectified versions of the velocity. The resulting functions for the contraction component of the velocity, $v_C(t)$, and the lengthening component of the velocity, $v_L(t)$, are shown in Fig. 6(a).

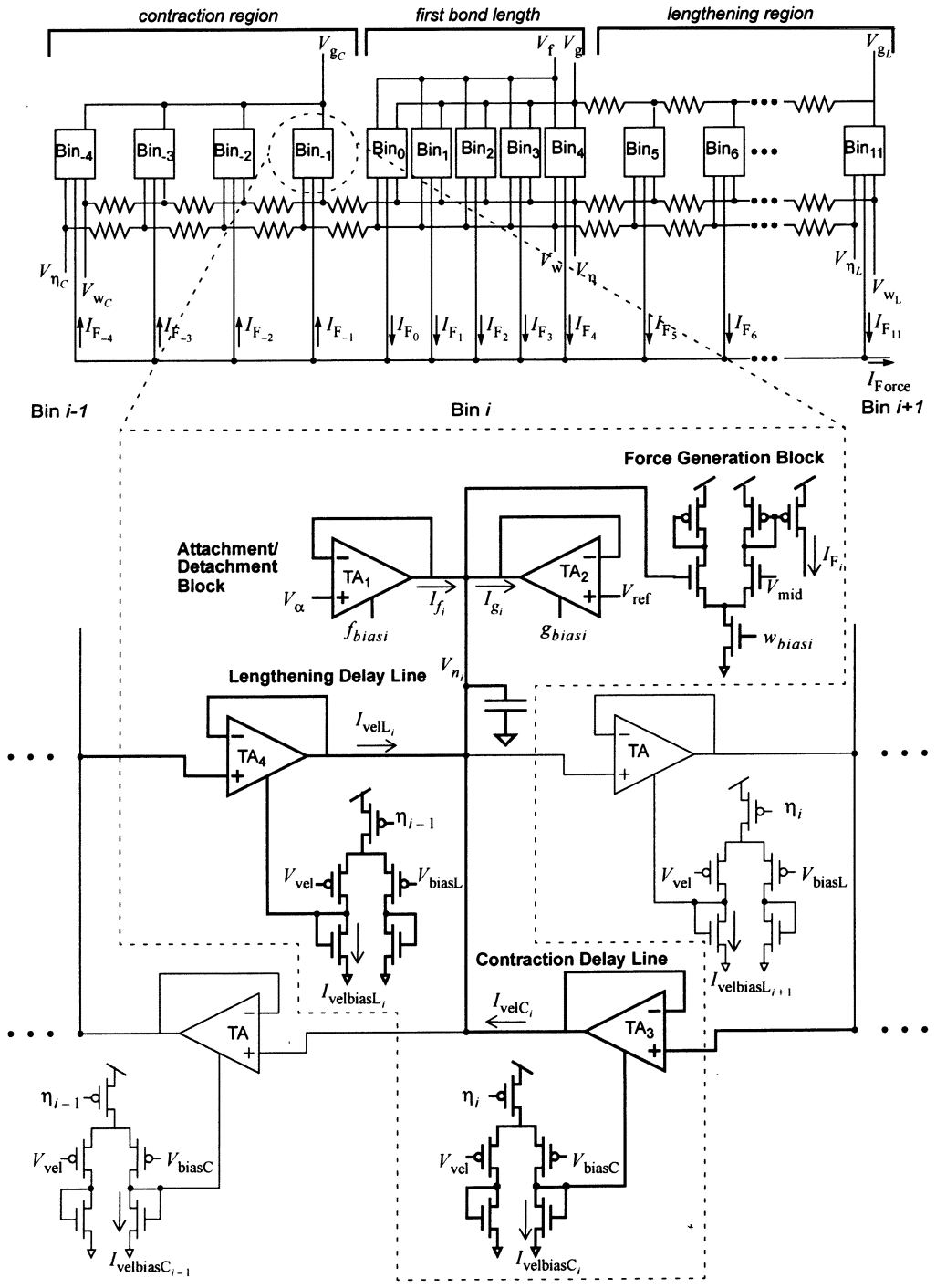

Fig. 5. Circuit diagram of a single bin implementing (3), with bold lines indicating the circuit elements comprising a single bin. TA_1 and TA_2 generate currents representing crossbridge attachment and detachment, while TA_3 and TA_4 are elements in delay lines that implement the translation of crossbridges as a function of velocity. The capacitor voltage V_{n_i} (representing the percentage of attached crossbridges in the bin), is translated into a current I_{F_i} (representing the force produced by the bin) by the differential pair in the *Attachment/Detachment Block*.

The discrete Huxley equation was rewritten as follows to include the half-wave rectified version of the velocity

$$\frac{d}{dt}n_i(t) = f_i(1-n_i(t)) - g_i n_i(t) + \begin{cases} v_C(t)\eta_i(n_{i+1}(t)-n_i(t)) \\ v_L(t)\eta_{i-1}(n_{i-1}(t)-n_i(t)) \end{cases} \quad (9)$$

where $\eta_i \equiv 1/(x_{i+1}(t)-x_i(t))$. The parameter η_i indicates the coupling strength among neighboring bins for a given velocity. Larger bins widths result in smaller coupling strengths and vice versa.

Each delay line is constructed using a set of TAs configured as unidirectional resistive elements (TA_3 and TA_4 in Fig. 5), which calculate the difference between neighboring capacitor voltages $V_{n_{i+1}} - V_{n_i}$. Similar to TA_1 and TA_2, if $V_{n_{i+1}} - V_{n_i}$ is less than 200 mV, the TAs operate in the linear portion of their transconductance relationship. V_α and V_{ref} constrain V_{n_i} to have a 200 mV range; therefore $|V_{n_{i+1}} - V_{n_i}| \leq 200$ mV

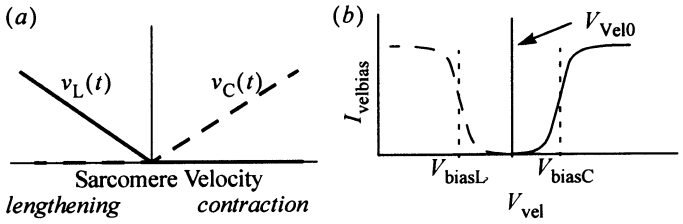

Fig. 6. Decomposition of the velocity term in order to ensure that crossbridge movement occurs in only one direction during a given length change. (a) Ideal decomposition, separating lengthening and contraction velocity components. When one function is nonzero, the other is zero. (b) Illustration of actual decomposition implemented by the differential pairs in the delay lines. Solid line shows $I_{\mathrm{velbias}\,C}$ for the contraction delay line. Dashed line shows $I_{\mathrm{velbias}\,L}$ for the lengthening delay line. This decomposition retains a region, V_{Vel0}, where both delay lines are inactivated.

and the TAs have a linear relationship between $V_{n_{i+1}} - V_{n_i}$ and $I_{\mathrm{vel}\,L_i}, I_{\mathrm{vel}\,C_i}$.

The dependence of the velocity term upon $v(t)$, represented by V_{vel} in the circuit, and η_i, is found in the formulation of $I_{\mathrm{velbias}\,L_i}$ and $I_{\mathrm{velbias}\,C_i}$. These two bias currents are generated by a differential pair, which has a sigmoidal relationship between its output current and its differential input voltage. If the differential input voltage is less than 200 mV, then the output current can be approximated by the following linear equations:

$$I_{\mathrm{velbias}\,L_i} = \frac{I_{\eta_{i-1}}\kappa}{4U_t}(V_{\mathrm{bias}\,L} - V_{\mathrm{vel}}) + \frac{I_{\eta_{i-1}}}{2} \tag{10}$$

$$I_{\mathrm{velbias}\,C_i} = \frac{I_{\eta_i}\kappa}{4U_t}(V_{\mathrm{vel}} - V_{\mathrm{bias}\,C}) + \frac{I_{\eta_i}}{2} \tag{11}$$

where I_{η_i} is the current through the bias transistor due to the bias voltage η_i and $V_{\mathrm{bias}\,L}$ and $V_{\mathrm{bias}\,C}$ are constant voltages that determine the zero velocity point of the circuit. The output current is taken from the respective opposite legs of the differential pair for the lengthening delay line versus the contraction delay line, producing opposite slopes for the output currents, as shown in Fig. 6(b).

The values for $V_{\mathrm{bias}\,L}$ and $V_{\mathrm{bias}\,C}$ are chosen such that $(V_{\mathrm{bias}\,C} - V_{\mathrm{bias}\,L}) = 200$ mV. This restriction ensures that only one delay line will be activated with a nonzero value of I_{velbias_i} for any given value of V_{vel}. Additionally, this separation between $V_{\mathrm{bias}\,L}$ and $V_{\mathrm{bias}\,C}$ creates a region where $I_{\mathrm{velbias}\,L_i} = I_{\mathrm{velbias}\,C_i} = 0$. This dead zone is necessary to ensure that some value for V_{vel} exists where neither delay line is activated, denoted by V_{zeroVel}. We can compute the final velocity terms, linearly dependent upon $V_{n_{i+1}} - V_{n_i}, V_{\mathrm{vel}}$, and η_i, as follows:

$$I_{\mathrm{vel}\,L_i} = \frac{\kappa}{2U_t}\left(\frac{I_{\eta_{i-1}}\kappa}{4U_t}(V_{\mathrm{bias}\,L} - V_{\mathrm{vel}}) + \frac{I_{\eta_{i-1}}}{2}\right) \times \left(V_{n_i} - V_{n_{i+1}}\right) \tag{12}$$

$$I_{\mathrm{vel}\,C_i} = \frac{\kappa}{2U_t}\left(\frac{I_{\eta_i}\kappa}{4U_t}(V_{\mathrm{vel}} - V_{\mathrm{bias}\,C}) + \frac{I_{\eta_i}}{2}\right) \times \left(V_{n_{i+1}} - V_{n_i}\right). \tag{13}$$

The resulting percentage of attached crossbridges for each bin, V_{n_i}, is weighted and translated into a current that represents the force contribution of a single bin, I_{F_i}. I_{F_i} is calculated in a similar manner as seen in (4). Each bin has a weight associated with the center of the bin. The weight parameter is calculated as $w_i = x_i \cdot \triangle x_i$, where $\triangle x_i$ is the width of the bin. w_i is encoded as the subthreshold bias current of a differential pair.

Because V_{n_i} is constrained to a 200 mV range, we can also assume that the weight differential pair is operating in its linear region. Thus, the output current of the bin, I_{F_i}, which represents the force generated by the bin, can be calculated as

$$I_{F_i} = \frac{I_{w\,\mathrm{bias}_i}\kappa}{4U_t}(V_{n_i} - V_{\mathrm{mid}}) + \frac{I_{w\,\mathrm{bias}_i}}{2} \tag{14}$$

where $I_{w\,\mathrm{bias}_i}$ is the bias current of the differential pair that results from the voltage w_{bias_i}. The parameter V_{mid} is set to a value of $(V_\alpha + V_{\mathrm{ref}})/2$ to ensure that there is a linear transformation between V_{n_i} and I_{F_i}. Due to the sigmoidal nature of the differential pair, this value of V_{mid} produces zero current when the capacitor voltage is equal to V_{ref}. If the bin has a negative x_i, the output current of the differential pair is copied by a current mirror so that bins with a positive value for x_i source current and the bins with a negative x_i sink current. The bin currents (which represent the force produced by each bin) are summed to compute the total sarcomere force as follows:

$$I_{\mathrm{Force}} = \sum_{i=0}^{k-1} I_{F_i}. \tag{15}$$

B. Parameter Distribution Among the Bins

The sarcomere circuit consists of sixteen bins connected in a distribution similar to one shown in Fig. 4. Five bins of equal bin width are placed in the first bond length, where $f_i > 0$. Seven bins of increasing bin width are placed in the lengthening region. Four bins of increasing bin width are placed in the contraction region.

Each bin has a number of bias voltages, including $V_\alpha, V_{\mathrm{ref}}, f_{\mathrm{bias}_i}, g_{\mathrm{bias}_i}, w_{\mathrm{bias}_i}, V_{\mathrm{mid}}, V_{\mathrm{vel}}, V_{\mathrm{bias}\,C}, V_{\mathrm{bias}\,L}$, and η_i. The level of sarcomere activation, V_α, and the sarcomere velocity, V_{vel}, are global inputs into each bin across the array. $V_{\mathrm{ref}}, V_{\mathrm{mid}}, V_{\mathrm{bias}\,C}$, and $V_{\mathrm{bias}\,L}$ are global constants used to bias all of the bins into the proper operating region. f_i, g_i, w_i and η_i are parameters that depend upon x_i, and therefore the bias voltages $f_{\mathrm{bias}_i}, g_{\mathrm{bias}_i}, w_{\mathrm{bias}_i}$ and η_i must be set differently for each bin. Setting these four bias voltages individually for each bin would require 64 inputs, requiring more than the 40 pins available on a standard tiny-chip. These voltages could be set by storing the values on the chip; however, when the sarcomere is one of many comprising a fiber, setting 64 bias voltages for every sarcomere would be tedious and difficult. Therefore, we applied other techniques to reduce the number of inputs from 64 to 10.

In the first bond length, we used a uniform distribution of bin widths equal to one-fifth the bond length. We achieved this uniform distribution by using a single input, V_η, to set all of the η_i voltages in this region, as shown in Fig. 5. We implemented the linear distribution of the f_i, g_i, and w_i parameters by linearly scaling the W/L ratios of the bias transistors in the corresponding TAs. This scaling allows the f_i, g_i, and w_i parameters

to be set for the entire region using only three bias voltages, V_f, V_g, and V_w.

In the lengthening region, $f_i = 0$, the slope of $g(x)$ increases, and the bin widths, and therefore the weights, increase monotonically in x, as shown in Figs. 3 and 4. The parameter f_i was set to zero in this region by connecting the nFET bias transistor of TA_1 to ground. We could have increased the remaining parameters by scaling the W/L values as seen previously; however this method would result in prohibitively large transistor sizes. Therefore, we used resistive ladders for each of the remaining parameters to produce linear gradients in the bias voltages for each of the TAs in this region, as shown in Fig. 5. If the voltages across the resistive ladder are below the threshold voltage of the transistors they are controlling, this linear gradient in bias voltage translates to an exponential gradient in bias currents.

The parameter η_i sets the bin width, and therefore the bin distribution. By connecting V_η to the left side of a resistive ladder and a new parameter, V_{η_L}, to the right side of a resistive ladder, we can control the distribution of bin widths in this region while preventing a discontinuity in bin widths between the first bond length and lengthening region. If V_{η_L} is closer to the power supply than V_η, the coupling between neighboring bins will decrease in x, producing an increasing distribution in bin center values, x_i, and therefore bin widths that increase exponentially.

Similarly, by connecting V_g to the left-hand side of the detachment rate resistive ladder and a new parameter, V_{g_L}, to the right-hand side, the bias currents of the detachment rate TAs will increase exponentially while preventing a discontinuity between the two regions. However, due to the manner in which η_i is being set, the x_i values are increasing exponentially in this region as well. Therefore, if the x_i distribution is carefully matched to the distribution of g_i values, $g(x)$ can increase linearly. The exact distribution of $g(i)$ values in this region is of the following form.

$$I_{g\,\mathrm{bias}_i} \approx x^{\frac{g_L - g}{\eta_L - \eta}}. \tag{16}$$

The weight parameter is defined as x_i multiplied by the bin width. Both x_i and the bin widths increase exponentially, therefore the weight parameter should increase exponentially as well. Again, we use a single resistive line to produce an exponential distribution. Similar to the η_i and g_i parameters, continuity between the two regions is maintained by connecting the left-hand side of the resistive ladder to V_w and the right-hand side of the ladder to a new parameter, V_{w_L}, that controls the weight distribution.

The contraction region parameters η_i and w_i are set in a similar manner using two additional resistive nets and the parameters V_{η_C} and V_{w_C} connected to the left-hand side of the coupling and weight resistive ladders, respectively. The detachment parameter is constant in this region. To obtain this relationship, we connected all the bias transistors of the detachment TAs to a single parameter V_{g_C}.

By utilizing resistive ladders and transistor scaling, we are able to control the entire 16-bin sarcomere using ten bias voltages. For proper circuit operation, all of the parameters must be set so that the bias transistors are operating in the subthreshold regime. In addition, the following constraints must be placed upon the parameters:

$$V_f > V_g \tag{17}$$

$$V_{g_L}, V_{g_C} > V_g \tag{18}$$

$$V_{w_L}, V_{w_C} > V_w \tag{19}$$

$$V_{\eta_L}, V_{\eta_C} > V_\eta \tag{20}$$

Using these parameter constraints, we have implemented and tested the operation of the circuit shown in Fig. 5, showing the effects of the delay line and crossbridge attachment and detachment rates on the force output [11].

The sarcomere model exhibits some second order phenomena. The linear assumption of (5) exhibits approximately 20% error when V_{n_i} is near V_α or V_{ref}. As a consequence, the implementation will allow a greater amount of charge to leave the bins in the first bond length during a lengthening or stretch after an isometric activation (where the length has not changed for a period of time and therefore all capacitor voltages have reached their maximum, (V_α)). This effect is due to a smaller tranconductance of the attachment TAs when the input is near V_α. Similarly, the detachment TAs will exhibit a lower transconductance when V_{n_i} is near V_{ref}. This voltage is observed most commonly in the lengthening and contraction regions before a change in length causes the charge to redistribute among the bins in this region. Thus, during contractions, the smaller transconductances will cause the charge to spread further down the delay line for the VLSI implementation than for the ideal mathematical model, resulting in a slightly lower final force. During lengthening, the effects of the attachment TAs in the first bond length and the detachment TAs in the lengthening region counter one another. Therefore, the effect is minimal, although it tends to lean toward slightly higher forces due to the higher weight distribution in the lengthening region.

Another second-order phenomena occurs if mismatch or poorly set parameters allows the lengthening delay line and the contraction delay line to be activated simultaneously. In this circumstance, the circuit can exhibit feedback loops between adjacent bins. As a consequence, as V_{n_i} increases due to a contraction, it drives its neighboring bin $V_{n_{i-1}}$ through the contraction delay line. As $V_{n_{i-1}}$ increases, it drives V_{n_i} through the lengthening delay line. This feedback continues until all node voltages reach the supply voltage. This effect is eliminated by the dead zone, described in Section IV.A. Additionally, this effect can be compensated by increasing the transconductance of the attachment and detachment TAs, which overpower the positive feedback in the delay line.

Finally, the delay line may exhibit offset accumulation if offsets occur in the same direction down the resistive ladders. This could potentially result in less or greater coupling between neighboring bins, which could effect the final force production. However, this phenomena does not have a significant effect on the qualitative behavior of the circuit.

C. Translation From Length to Activation

There are three major circuits in our system that transform the sarcomere length in order to accurately reflect the effects of

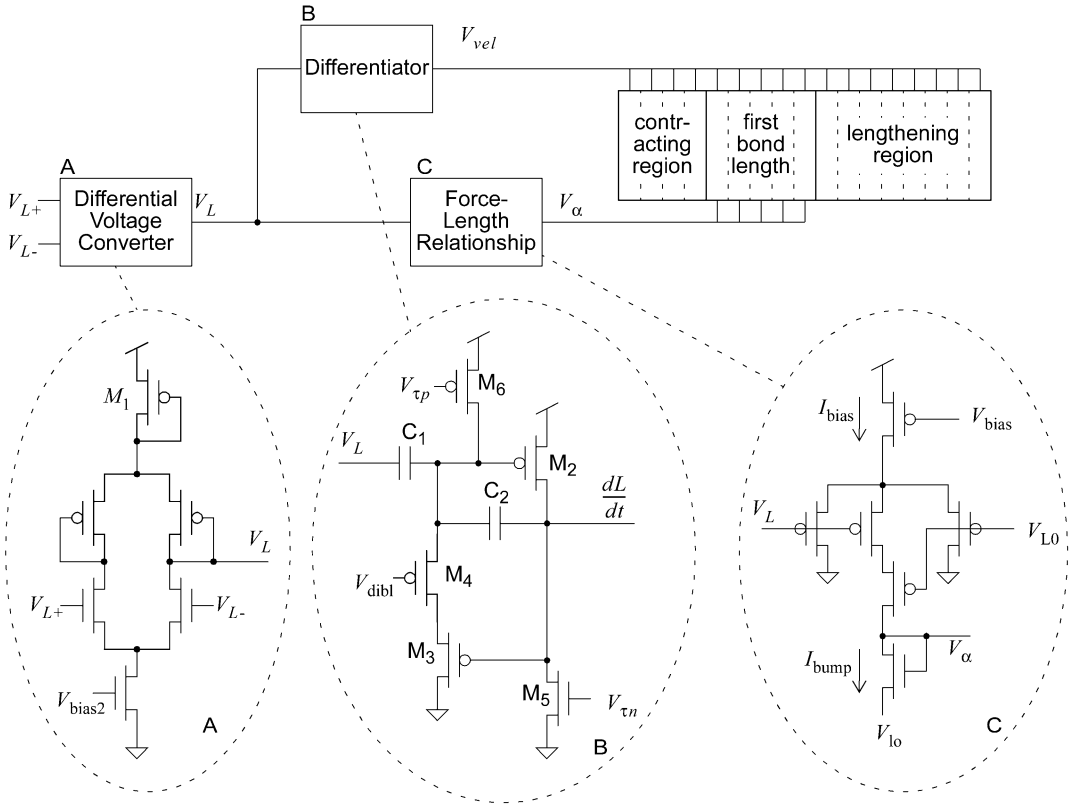

Fig. 7. Schematic of the circuits used to transform sarcomere length changes into velocity and activation terms. The differential voltage converter shown in A translates the differential voltage $V_{L+} - V_{L-}$ into a single-ended voltage V_L representing the sarcomere length. The differentiator shown in B (a C^4 circuit [12]) generates the temporal derivative of V_L; its output voltage $V_{\rm vel}$ represents the sarcomere velocity. The force–length circuit shown in C (a modified bump circuit [13]) translates V_L into a voltage V_α representing the number of crossbridges able to bind.

sarcomere length on force output. A differential-to-single-ended voltage converter allows us to express sarcomere length as a differential voltage, facilitating the future development of fiber models. A differentiator transforms the length into the velocity term $V_{\rm vel}$. Additionally, a bump circuit transforms the length into an activation factor, V_α, reflecting how sarcomere length effects the total number of crossbridges available for attachment. These circuits are illustrated in Fig. 7.

In order to facilitate the future development of a muscle fiber comprised of several sarcomeres in series, we chose to represent sarcomere length with a differential signal. In order to meet later processing stages' requirement of a single-ended voltage representing length, we designed a differential-to-single-ended voltage converter (block A in Fig. 7) to transform the differential length, $V_{L+} - V_{L-}$, into V_L. The additional diode connected pFET, M1, in the converter ensures that the maximal value of V_L will be approximately $V_{\rm DD} - V_{\rm bias2}$. This lowering of V_L below the supply voltage ensures that it will remain in the common-mode input range of the next stage.

To transform the length V_L into a velocity, we designed a differentiator circuit (block B in Fig. 7) using a Capacitively Coupled Current Conveyer (C^4) [12]. The C^4 can be used as a bandpass filter with adjustable corner frequencies. By operating on the ascending leg of the C^4's bandpass filter, we generate the differential function. This creates a compact differentiator that does not demonstrate ringing, which is essential for a true velocity calculation. In addition, the circuit can produce a gain of less than one at low frequencies. These factors made the C^4 attractive for our design.

One limitation of the C^4 circuit is its nonlinear response to a step increase in V_L. The transistor M4, a drain induced barrier lowering (DIBL) FET, helps to linearize this response [12]. The gate of M4 is less than the minimum length, which produces a large amount of channel-length modulation. When we hold the gate of M4 at a constant voltage, channel-length modulation modulates the current through M3, linearizing the operating range.

The force–length relationship (block C in Fig. 7) was computed using a "bump" circuit [13], which has a nonlinear transfer function that is qualitatively similar to the biological force–length relationship. This circuit has two inputs representing the length of the sarcomere, V_L, and the optimal length of the sarcomere (the length at which maximal force is produced), V_{L0}. When these two values are equal to one another, the bias current is shared equally among all branches, generating the maximal value of the output current, $I_{\rm bump}$. As V_L and V_{L0} differ from one another, the gain of one of the two series transistors is reduced, lowering the value of $I_{\rm bump}$. Thus, as the differential voltage increases, the output current falls to zero.

The output current is translated into a voltage, V_α, using a diode connected transistor. The diode connected transistor has a logarithmic relationship between input current and output

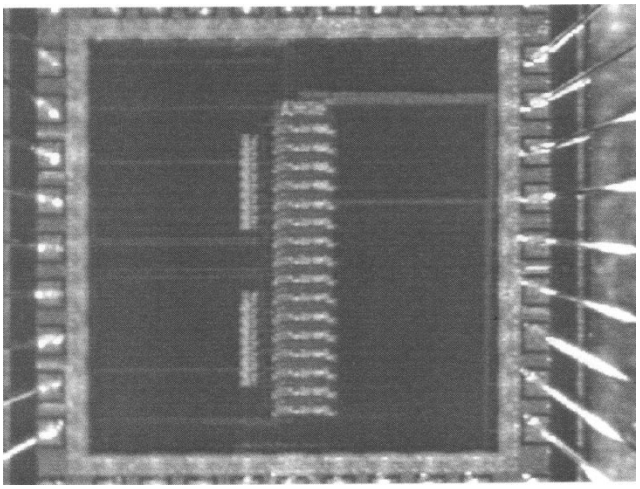

Fig. 8. Photograph of the sarcomere circuit model, fabricated in a 1.2 μm process on a 1500 μm $\times$ 1500 μm TinyChip. The sarcomere circuit itself measures 292 μm $\times$ 1300 μm (379 600 μm^2).

voltage, which results in a compression of the output voltage. V_α is computed as follows.

$$V_\alpha = \frac{U_T}{\kappa} \ln \left[I_{\text{bias}} \frac{1}{1 + 4\cosh^2\left(\frac{\kappa \triangle V}{2}\right)} \right]. \qquad (21)$$

The logarithmic compression produces a rising and falling slope that behaves linearly over the input range and broadens the region for the peak voltage. The output range is limited due to this logarithmic compression; however the sarcomere circuit requires only a 200 mV range for V_α. Therefore, the logarithmic compression improves the qualitative matching of the circuit to the sarcomere data [1], [7]. When $V_L = V_{L0}, V_\alpha$ reaches its maximal value, producing the maximal force in the sarcomere. The maximal value of V_α is controlled by the bias current, which is set by V_{bias}. The source voltage of the diode connected transistor is connected to a bias voltage, V_{lo}. V_{lo} constrains the lower boundary of V_α within the common-mode input range of the sarcomere TAs. The value of V_{L0} may be modified to change the input voltage necessary to produce the peak force, which allows us to vary the force–length characteristic of sarcomeres in an array.

V. Experimental Results

We fabricated the sarcomere circuit using the Mosis fabrication facility using the AMI 1.2-μm CMOS process. In this process, a single sarcomere circuit requires an area of 292 μm $\times$ 1300 μm (379 600 μm^2). Roughly 30% of this area consists of bin capacitors. A photograph of the fabricated chip is shown in Fig. 8. Initially, we obtained experimental measurements of the effects of the force–length relationship circuit and the differentiator on the force current individually to understand their individual contributions to the force. Then we measured the force response with both circuits activated.

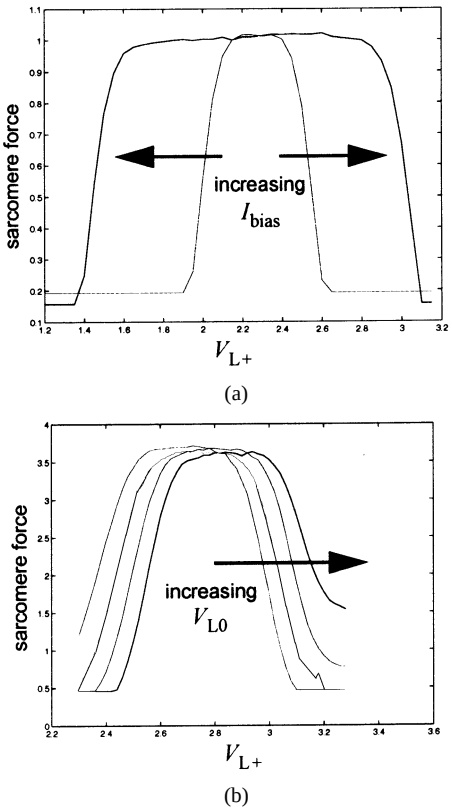

Fig. 9. Experimental data showing the force–length relationship of the length-dependent sarcomere. (a) Increasing I_{bias} broadens the force–length curve. (b) Changing V_{L0} translates the the force–length curve, changing the length at which maximum force is generated.

A. Force–Length Relationship

The force–length characteristic of the circuit was measured for different values of V_{bias} and V_{L0} (refer to Fig. 7 for the circuit schematic). V_{L+} was swept over a range of values while V_{L-} was held at a constant voltage. The sum of all bin currents, I_{Force}, was measured using a current-to-voltage converter driving an oscilloscope. The effects of the velocity circuits were eliminated by placing the bias voltages for the velocity circuits, $V_{\text{bias}\,L}$ and $V_{\text{bias}\,C}$, high and low respectively, which set the bias currents for the velocity TAs to zero.

Fig. 9(a) presents the force–length relationship for two different values of the bump circuit bias voltage, V_{bias} (refer to Fig. 7 for the circuit schematic). The curves have been normalized by their maximal output voltages so that the shapes of the two different curves may be compared. The broader curve is due to a larger value of I_{bias}. Increasing the bias current of the bump circuit increases the operating range of V_α, which increases the range of lengths over which the circuit produces a nonzero force. Both curves exhibit a flat plateau region around the optimal length, which is uncharacteristic of the bump circuit. This plateau region is due to the limited range of operation of the sarcomere circuit. The TAs in the sarcomere circuit have a linear input-output relationship for only 200 mV. Therefore, if the range of V_α is greater than 200 mV, the TAs in the sarcomere circuit saturate. In this region of operation, V_α has no effect on the circuit. While initially this limitation in operating range may appear as a limitation of the circuit, in practice it broadens the plateau region, producing a force–length curve

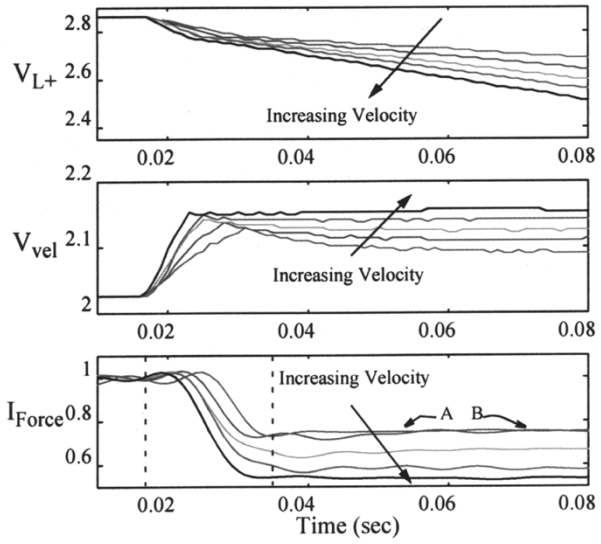

(a)

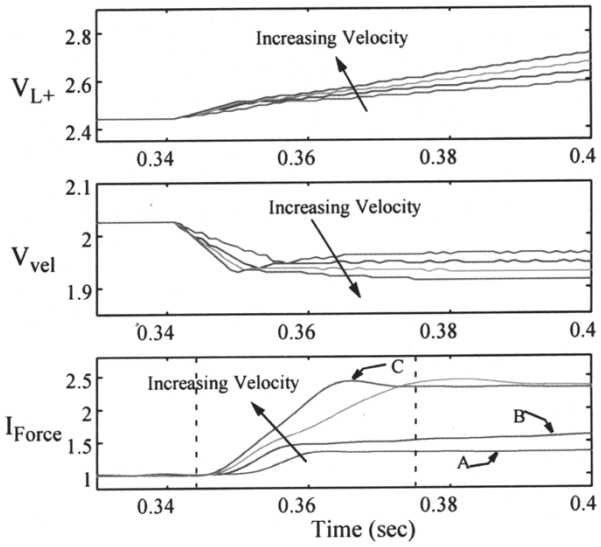

(b)

Fig. 10. Transient force output of the sarcomere circuit shown in Fig. 7 with length circuitry inactivated. (a) Response to constant-velocity contractions. (b) Response to constant-velocity stretches. In both figures, the top graph indicates sarcomere length, the middle graph indicates the output of the length differentiator circuit, and the bottom graph indicates sarcomere force output.

that is better matched to the biological data [1], [7]. The effects of modifying the optimal length, V_{L0}, are demonstrated in Fig. 9(b). Increasing the value of V_{L0} shifts the force–length curve to the right, but has no effect on the shape of the curve.

B. Force–Velocity Relationship

The effects of different velocity contractions and stretches is demonstrated in Fig. 10(a) and (b). In this experiment, we controlled the input V_{L+} with a decreasing or increasing ramp function (representing a constant-velocity contraction or a stretch respectively) while holding V_{L-} at a constant voltage. We repeated the experiment with ramps changing at rates of 2.21, 2.94, 3.98, 4.37, and 5.17 V/s. Using an oscilloscope, we measured the output of the C^4, $V_{\rm vel}$, and the force of the sarcomere, $I_{\rm Force}$. The top graph in the figure presents V_{L+}, the middle $V_{\rm vel}$, and the bottom $I_{\rm Force}$. In order to ensure that we did not move into the pass-band region of the C^4 circuit, we operated the circuit in the lower region of the ascending limb of the band-pass transfer function. As a result, the gain was very low and the C^4 responded slowly. To compensate for this problem, we used a nonlinear ramp function. Initially, the ramp has a higher slope to force the C^4 circuit to respond, then the ramp function slows down to the desired slope.

The C^4 circuit produces a step function in response to the ramp input, demonstrating the effectiveness of the circuit in producing derivatives. Both stretches and contractions produce step functions with similar differential voltage levels and similar time constants. As the speed of the contraction or stretch increases (shown by an increase in the slope of the line V_{L+}), the steady-state value of $V_{\rm vel}$ increases. The overshoot in $V_{\rm vel}$ is due to the slope change in the nonlinear ramp function used to force a quick response from the C^4 circuit.

The sarcomere circuit produces nonlinear force responses in response to the step in $V_{\rm vel}$, as shown in Fig. 10(a). The force data is normalized to the force production of the sarcomere at zero velocity (called the isometric force). In response to a contraction, each curve demonstrates an exponential decay (shown between the dashed lines) down to a steady-state force (shown after the second dashed line). This same response has been demonstrated in biological muscles [5]. The explanation of this effect can be observed by investigating the steady-state form of the Huxley equation.

$$\frac{d}{dx}n(x) = \frac{f(x)+g(x)}{\rm vel} - \frac{f(x)}{\rm vel}. \tag{22}$$

The solution of (22) in the first bond length is of the form

$$n(x) = Ae^{(\frac{f+g}{2{\rm vel}})x^2} + B. \tag{23}$$

Thus, the bond distribution in the first bond length decreases exponentially with the velocity, causing the force to decrease exponentially. The solution of (22) in the contraction region is of the form

$$n(x) = Ae^{(\frac{g_3}{\rm vel}x)}. \tag{24}$$

Because x is negative in this region, the bond distribution increases exponentially with velocity, causing the force to decrease exponentially. Assuming that our circuits are operating in the linear regions of the TAs, they should produce a similar result.

Increasing the velocity of contraction results in lower steady-state force and an increase in the slope of the initial fall in force, which qualitatively matches biological data [5], [14]. Note that for higher velocity contractions, the force reaches its steady-state after the velocity reaches its plateau, indicating that the interactions between velocity current, attachment current, and detachment current are responsible for the development of steady-state force.

In response to a stretch, as shown in Fig. 10(b), each curve demonstrates a rapid increase in the current representing force (shown between the two dashed lines) until a new steady-state force is reached (shown after the second dashed line). As the velocity is increased, the slope of the initial rise in force and

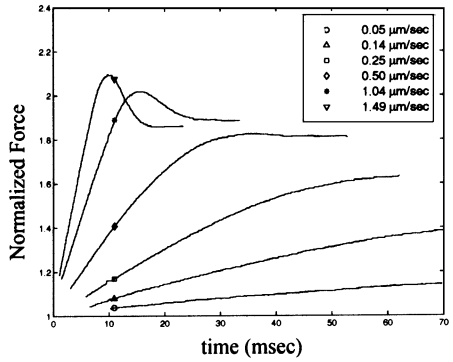

Fig. 11. The force output of a biological muscle (frog sartorius) in response to stretches at six different velocities (from [14]). This data compares well qualitatively to the force output of the sarcomere circuit shown in Fig. 10(b).

the steady-state force both increase until a phenomenon known as yielding occurs, as demonstrated by curve C. In yielding, a lengthening muscle transiently generates a peak force that is greater than its steady state force at that velocity. Fig. 11 shows yielding behavior in a muscle fiber from the sartorius muscle of the frog in response to a step increase in velocity [14]. The two diagrams present similar behaviors. As velocity increases, the steady-state force increases and yielding becomes evident. The biological data demonstrates a larger change in the slope of the initial response than the circuit data. We believe our circuits could demonstrate a similar behavior by modifying the parameters.

The experimental data does not perfectly replicate the ideal simulation of the model. The steady-state force shown by curves A and B in both the contraction and lengthening graphs do not exhibit much variation from one another. This effect is due to the nonlinearity of the circuits converting the velocity to the bias currents controlling the delay lines (see Fig. 5). These differential pairs exhibit a sigmoidal relationship between $V_{\rm vel}$ and $I_{\rm velbias\,L_i}$. As a consequence, the delay line is not activated as strongly at very high and very low velocities. Additionally, the force in this circuit is overestimated for lengthenings and underestimated for contractions. These errors can be corrected by adjusting the parameters of the circuit.

C. Interaction of Velocity and Length

The final set of experiments investigated the effects of the interaction between the length and velocity on sarcomere force. The experimental procedures were similar to the velocity tests. We controlled the input V_{L+} with a decreasing or increasing ramp function (representing a constant-velocity contraction or a stretch respectively) while holding V_{L-} at a constant voltage. Using an oscilloscope, we measured the output of the bump circuit, V_α, and the force of the sarcomere, $I_{\rm Force}$.

To better understand what is expected of the data in this section, we will first reexamine the circuit model. V_α only effects capacitor voltages in the first bond length. Without the effects of the velocity on the bin distribution, the force would merely follow V_α. However, the velocity delay line causes charge to move out of the first bond length and into the lengthening or contraction regions where V_α has no effect. Greater velocities cause more charge to move out of the first bond length. Therefore, we would expected the force response of low velocity con-

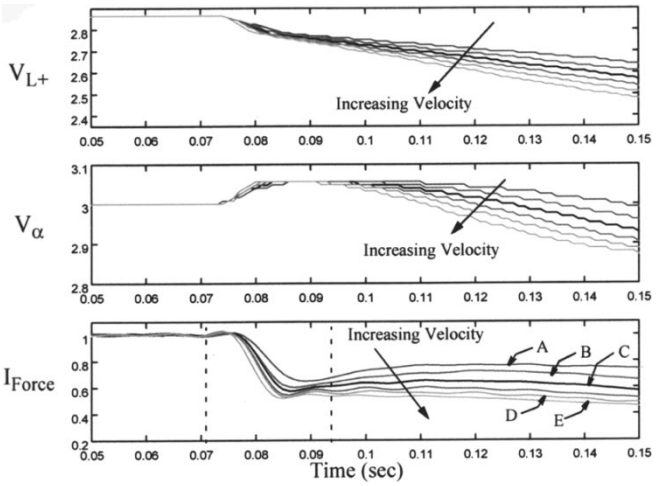

(a)

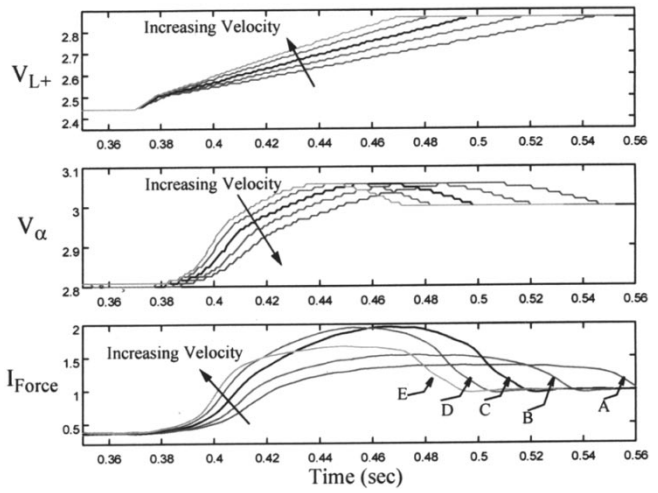

(b)

Fig. 12. Force output of the sarcomere circuit shown in Fig. 7 with length circuits activated. (a) Response to constant-velocity contractions. (b) Response to constant-velocity stretches. In both figures, the top graph indicates sarcomere length, the middle graph indicates the output of the force–length circuit, and the bottom graph indicates sarcomere force output. The force demonstrates characteristics of both the force–length and force–velocity relationships.

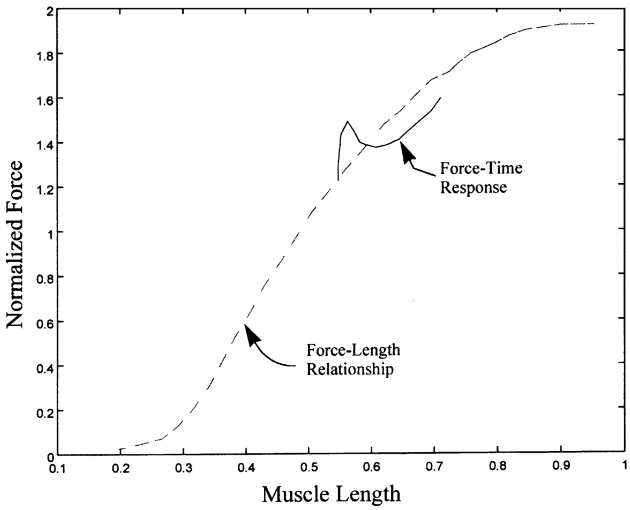

Fig. 13. Force response of soleus in response to a lengthening [1], [7]. The muscle is stretched far enough to exhibit both velocity and length characteristics. Dashed line represents the force–length relations of the muscle. The data qualitatively matches the experimental data shown in Fig. 12.

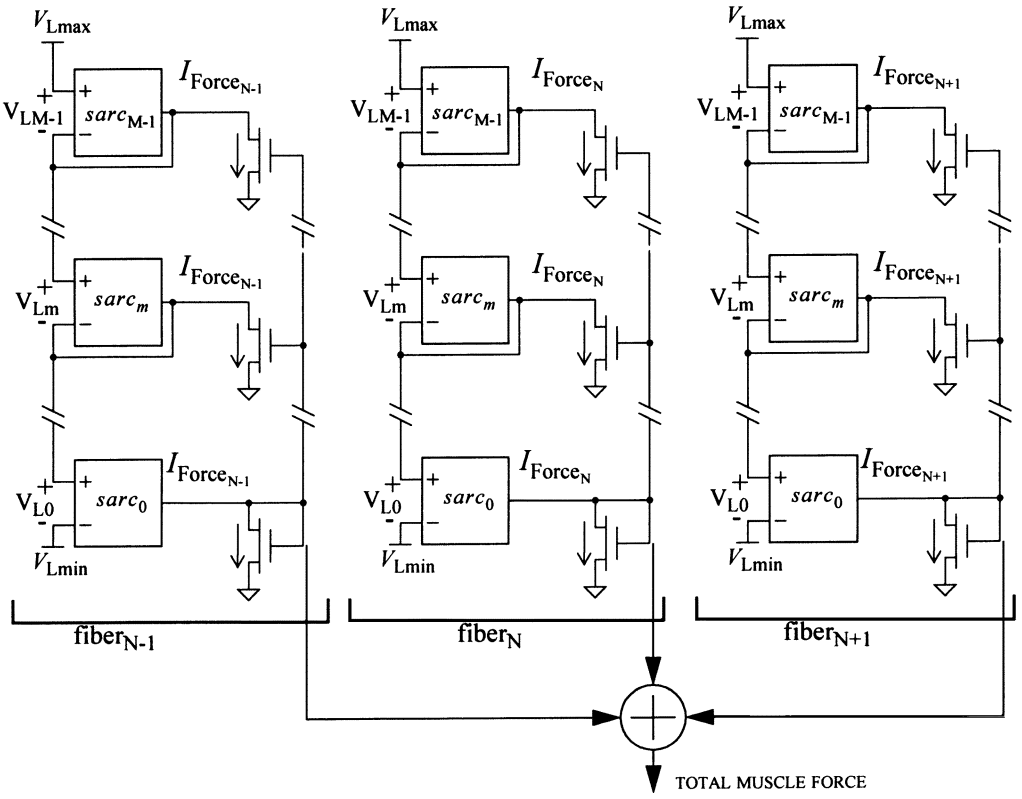

Fig. 14. System of sarcomeres connected in series (sharing the same force) and in parallel (sharing the same total length) to model a whole muscle.

tractions and lengthenings to appear much like V_α. The force response of high velocity contractions and lengthenings should appear much like the data shown in Fig. 10.

Fig. 12(a) and (b) present the effects of contractions and stretches at the rates of 2.21, 2.94, 3.98, 4.37, 5.17, and 6.32 V/s on the force. The top graph in the figure presents V_{L+}, the middle V_α, and the bottom $I_{\rm Force}$. As the length decreases (a contraction), V_α also decreases, indicating that bump circuit is operating on the ascending limb of the force–length relationship. Similarly, when the length increases (a stretch), V_α increases, also indicating that the bump circuit is operating on the ascending limb. As demonstrated in Fig. 9, the general shape of V_α does not depend on the velocity, but only the length. The force, however, is sensitive to both velocity and length.

Fig. 12(a) presents the effects of the velocity and length mechanisms on the force in response to contractions at different velocities. The region between the dashed lines shows a sharp decline in the force due to the velocity circuits. This decline represents the initial transient response of the muscle to a contraction. In the region after the second dashed line, the velocity circuits have reached their steady state, which allows the length component to become evident for slow velocities. Note the small curvature of the force in this region as compared to the seady-state force in Fig. 10 (see curves A, B, and C). This small curvature is due to the length component of the circuit. At higher velocities (curves D and E), a larger percentage of the charge is moved out of the first bond length, which minimizes the effect of V_α on the force. Thus, less curvature in the steady-state region is demonstrated.

Fig. 12(b) demonstrates the effects of length and velocity on the force in response to different velocity stretches. Since both the length and velocity circuits increase the force under these circumstances, the force output resembles V_α more closely that the contraction data. The force follows the general shape of V_α; however the force is amplified by the velocity circuits. Higher velocities, which cause higher steady-state forces, result in greater amplification, as shown by curves A, B, C, and D of the force graph. The force amplification is reduced in the highest velocity stretch (curve E) due to force yielding.

This data does not seem to be consistent with the single fiber data presented in Fig. 11. However, this biological data was taken over a small length change occurring at the peak of the force–length relationship, where the force does not change with length. Responses similar to the data shown in Fig. 12 have been demonstrated by Joyce, Rack, and Westbury in whole muscle experiments [7] and are presented in Fig. 13, [1]. When cat soleus is stretched along the ascending leg of its force–length relationship (shown as a dashed line), the force increases and falls back to the isometric force mediated by the force–length curve. Similarly, when the muscle contracts in this same region, the force falls below the isometric force and saturates at the new isometric level. The biological data is qualitatively matches the experimental data shown in Fig. 12(b).

VI. Conclusion

We have developed a crossbridge-level model of sarcomere behavior using integrated circuits. By using a discrete form of the Huxley equation governing crossbridge interaction, we are

able to approximate its continuous spatial and temporal solution. By employing a nonlinear bin distribution, we are able to implement the discrete solution using only sixteen spatial bins. The output current representing force responds to a change in sarcomere length (represented as a differential voltage) and demonstrates many of the nonlinear mechanical characteristics observed in muscle, such as short-range stiffness, yielding, and the subtle interactions between length and velocity. These nonlinear characteristics would be difficult to produce without basing the model upon the underlying mechanisms governing crossbridge interaction. Thus, the implementation is a real-time model that produces biomorphic characteristics. Due to the ability of the model to simulate sarcomere behavior in real-time, it can be used in engineering systems to add biological properties to a standard linear actuator, producing a biomorphic actuator. Such an actuator, by producing a force that demonstrated the flexibility and complexities inherent in biological muscle, could be used in applications such as prosthetics and autonomous robotics.

To examine the efficiency of our analog model, we simulated Huxley's model with the same discrete, 16-bin nonlinear grid using a real-time digital emulation board driven by a DSP. This model achieved real-time behavior as well, running at a maximum speed of 1 kHz. The algorithm required approximately 4 MIPs. Assuming that the processor requires 1 mW for every 20 MIPs, the DSP processor would require approximately 200 μW to run the algorithm. Our analog implementation, running in the subthreshold regime, requires approximately 0.5 μW. These numbers suggest that the analog controller of a prosthetic or autonomous robot would run three orders of magnitude longer than a traditional DSP solution on the same power supply. The advantages of the analog model are further demonstrated when developing a model of a whole muscle. As shown in Fig. 1, muscles are comprised of many sarcomeres in series and parallel that interact with one another. The analog circuit model sarcomere may be implemented easily into an array, as shown in Fig. 14, to produce a whole muscle model. This type of model can be used to study the effects of low-level mechanics on the force characteristics of a highly parallel, distributed actuator, as well as providing insight into the effects of muscle architecture on biological motor control. While, the DSP may have difficulty emulating 100 or 1000 of these sarcomere models in real time, the parallel nature of the analog model allows this type of scaling to occur with ease. Using a 0.18-μm process, 100 sarcomere models could be placed on a 7-mm^2 die and 1000 sarcomere models could be placed in a 1-cm^2 die. Thus, such a highly parallel model of muscle is feasible using today's technology.

ACKNOWLEDGMENT

The authors would like to acknowledge D. C. Lin of the University of Washington and T. R. Nichols of Emory University for many detailed discussions about muscle physiology.

REFERENCES

[1] C. Ghez, "Muscles: Effectors of the motor system," in *Principles of Neural Science*, 3rd ed, E. R. Kandel, J. H. Schwartz, and T. M. Jessell, Eds. New York: Elsevier, 1991, pp. 548–563.

[2] J. M. Hollerbach, I. W. Hunter, and J. Ballantyne, "A comparative analysis of actuator technologies for robotics," in *Robotics Rev. 2*, O. Khatib, J. Craig, and T. Lozan-Perez, Eds. Cambridge, MA: MIT Press, 1991, pp. 299–342.

[3] C. Mead, *Analog VLSI and Neural Systems*. Reading, MA: Addison-Wesley, 1989.

[4] A. F. Huxley, "Muscle structure and theories of contraction," in *Prog. Biophys. Biophys. Chem.*, vol. 7, 1957, pp. 257–318.

[5] J. G. Malamud, R. E. Godt, and T. R. Nichols, "Relationship between short-range stiffness and yielding in type-identified, chemically skinned muscle fibers from the cat triceps surae muscles," *J. Neurophysiol.*, vol. 76, no. 4, pp. 2280–2289, 1966.

[6] A. Prochazka, D. Gillard, and D. J. Bennett, "Positive force feedback control of muscles," *J. Neurophysiol.*, vol. 77, no. 6, pp. 3226–3236, 1997.

[7] G. C. Joyce, P. M. H. Rack, and D. R. Westbury, "The mechanical properties of cat soleus muscle during controlled lengthening and shortening movements," *J. Physiol (Lond.)*, vol. 240, pp. 461–474, 1969.

[8] G. I. Zahalak, "A distribution-moment approximation for kinetic theories of muscular contraction," *Math. Biosci.*, vol. 55, pp. 89–114, 1981.

[9] W. E. Schiesser, *The Numerical Method of Lines: Integration of Partial Differential Equations*. San Diego, CA: Academic, 1991.

[10] T. A. Hudson, J. A. Bragg, E. A. Brown, D. C. Lin, and S. P. DeWeerth, "Development of a sarcomere model using hardware," in *Proc. Joint BMES/EMBS Conf.*, Oct. 1999, p. 89.

[11] T. A. Hudson, J. A. Bragg, D. C. Lin, and S. P. DeWeerth, "An integrated circuit implementation of the Huxley sarcomere model," *IEEE Trans. Biomed. Eng.*, vol. 48, pp. 1471–1479, Dec. 2001.

[12] P. Hasler, M. Kucic, and B. Minch, "A transistor-only circuit model of the autozeroing floating-gate amplifier," *Proc. IEEE Midwest Symp. Circuits and Systems*, pp. 157–160, Aug. 1999.

[13] T. Delbruck, "Bump Circuits for Computing Similarity and Dissimilarity of Analog Voltages," California Inst. of Technol., Pasadena, CNS Memo, May 1993.

[14] F. Colomo, V. Lombardi, and G. Piazzesi, "The mechanisms of force enhancement during constant velocity lengthening in tetanized single fibers of frog muscle," *Adv. Experiment. Med. Biol.*, vol. 226, pp. 489–502, 1988.

Tina A. Hudson (M'98) received the M.E.E. and Ph.D. in electrical engineering from Georgia Institute of Technology in 1995 and 2000, respectively.

She is an Assistant Professor in the Department of Electrical and Computer Engineering at Rose Hulman Institute of Technology. Her research interests include the development of real-time neuro-muscular models using integrated circuits and linear threshold circuits.

Julian A. Bragg (M'98) received the B.S. degree in electrical engineering from The George Washington University, Washington, DC, in 1995, and the Ph.D. in bioengineering from the Georgia Institute of Technology, Atlanta, in 2002. He is currently working toward the M.D. degree at the Emory University School of Medicine, Atlanta, GA.

His research interests include neuroscience, muscle physiology, and biological motor control.

Dr. Bragg is a member of Tau Beta Pi and Eta Kappa Nu.

Paul Hasler received the M.S. and B.S.E. degrees in electrical engineering from Arizona State University, Tempe, in 1991, and the Ph.D. degree from the California Institute of Technology, Pasadena, in computation and neural systems in 1997.

He is an Associate Professor in the School of Electrical and Computer Engineering at Georgia Institute of Technology. He has been with Georgia Institute of Technology since 1997. His current research interests include low power electronics, mixed-signal system ICs, floating-gate MOS transistors, adaptive information processing systems, "smart" interfaces for sensors, cooperative analog-digital signal processing, device physics related to submicron devices or floating-gate devices, and analog VLSI models of on-chip learning and sensory processing in neurobiology.

Dr. Hasler received the NSF CAREER Award in 2001, and the ONR YIP Award in 2002. He has received the Paul Raphorst Best Paper Award, IEEE Electron Devices Society, 1997, and Best Paper Award at SCI 2001.

Stephen P. DeWeerth (M'85) received the M.S. degree in computer science and the Ph.D. degree in computation and neural systems from the California Institute of Technology in 1987 and 1991, respectively. He is presently a Professor in the School of Electrical and Computer Engineering and in the Coulter Department of Biomedical Engineering at the Georgia Institute of Technology and the Emory University School of Medicine in Atlanta, Georgia. He is also the Director of the Center for Neuroengineering at Georgia Tech and Emory.

Prof. DeWeerth's research emphasizes the development of systems that are inspired by and interfaced to neurobiology. For much of his career, he has focused on the development of neuromorphic VLSI circuits and systems, specifically those that address sensorimotor processing, visual attention, and rhythmic motor control. His present research has expanded upon that focus to include the development of MEMS-based technology, multielectrode arrays (MEAs), and signal-processing circuitry for interfacing to neural tissue in vitro. The central theme of his present research is the development of hybrid neural microsystems: the integration of living neural tissue and real-time microelectronic circuitry in closed-loop configurations to address applications including the neural control of movement.